Three-Dimensional Computation of Flow Past Cylindrical Structures and Model Cooling Towers

S. MAJUMDAR*
W. RODI*

The paper reports on the application of a 3-D finite-volume method employing an orthogonal, cylindrical-polar body-fitted grid and the standard k–ε turbulence model to the calculation of flow and plume spreading past surface-mounted circular structures. Calculations are presented for two idealized laboratory situations, one being the flow around a circular cylinder of height-to-diameter ratio 1.9 immersed in a simulated atmospheric boundary layer and the other the flow past a model cooling tower with ratio of plume exit to cross-flow velocity of 1.67 and with an inert tracer added to study the plume spreading. Comparison with experimental results establishes the capability of the numerical model to reproduce many of the complex flow features in the vicinity of cylindrical structures and also of the plume spreading. Certain discrepancies between calculations and experiments point to the need for a more refined treatment of the boundary layer developing on the ground, a better numerical resolution, and the use of an H-grid instead of a polar grid when plume spreading is to be studied.

1. INTRODUCTION

THE DESIGN of safe and energy-efficient buildings that also have satisfactory environmental performance requires a predictive understanding of the interaction between the wind and the building. In particular, the designer needs to know the wind forces on the building and on various parts of it, the wind pattern developing around the building or between buildings, and the dispersion of pollutants emitted from buildings. With respect to the latter, an extreme case is a cooling tower with its associated thermal plume. In this example, the environmental impact of the emitted plume is of particular interest, i.e. the design engineer wants to know how the plume spreads under various meteorological conditions and how quickly the rejected waste heat will be diluted.

Usually, a predictive understanding of flow around buildings under design is obtained from scale-model studies carried out in wind or water tunnels. A single study of this kind is already very laborious, but parameter studies for optimizing the design are particularly unattractive as they are very time-consuming and expensive. Hence, there is a great need for reliable mathematical models with which, once the model has been set up and tested, parameter studies can be carried out much more easily, quickly and more cheaply.

The flow around buildings, which act as bluff obstacles placed in the atmospheric boundary layer, is always extremely complex, as described for example by Hunt *et al.* [1]. The flow is always 3-D, it separates from the

structure, and various vortex systems aligned in different directions are set up which interact with each other; in the case of taller buildings, the mean flow is usually not steady as periodic vortex shedding occurs [2]; superimposed is of course the unsteady turbulent motion. In the case of a cooling tower, the complexity of the flow is further enhanced due to the strong interaction between the discharged plume and the flow around the tower. If not only global parameters like drag coefficients need to be predicted, but also details on the complex flow around buildings, a mathematical model is required that is based on the 3-D Navier–Stokes equations. These equations can only be solved numerically with a very large number of arithmetic operations.

It was not until the early 70's that computers became powerful enough to attempt a solution of the Navier-Stokes equations for the 3-D problem of flow around idealised buildings. Since then, most calculations were carried out for steady flow around single buildings of rectangular shape. Of necessity, the earlier calculations employed rather coarse numerical grids and assumed either laminar flow or used only a crude representation of the turbulent transport processes, for example through a suitably adjusted constant eddy viscosity. This crude turbulence representation cannot do any justice to the complex turbulent shear layers developing in the flow around buildings. The first calculations performed with a more refined model of turbulence were those of Vasilic–Melling [3]. She employed the *k*–ε model, which determines the distribution of the eddy viscosity by solving additional transport equations for the turbulent kinetic energy *k* and the dissipation rate ε, and she used as test case the flow around a surface-mounted cube studied experimentally by Castro and Robins [4] both with uni-

*Institute for Hydromechanics, University of Karlsruhe, Karlsruhe, F.R.G.

form cross flow and an oncoming boundary layer. These calculations were followed by similar ones of Benodekar et al. [5], Paterson and Apelt [6] and Baetke [7, 8] with improved numerical methods and finer grids, but with the same k–ε turbulence model. The latter studies produced generally good agreement with the measurements of Castro and Robins concerning the velocity and surface pressure distribution. All the calculations discussed so far were of steady flow, solving the time-averaged Navier–Stokes equations. Murakami et al. [9] applied the large-eddy-simulation technique to calculate the flow around a surface-mounted cube. In this technique, the unsteady Navier–Stokes equations are solved, and periodic vortex shedding motion (if it exists) can be resolved as well as the large-scale part of the turbulent motion. Only the small-scale turbulent motion that cannot be resolved with a certain numerical grid has to be modelled by a so-called subgrid scale model. Murakami et al. obtained remarkable similarity between calculations and flow visualization and measurements even with a fairly coarse grid. Calculations of the flow around buildings with shapes other than rectangular are not known to the authors. In particular, there seem to be no calculations for the flow around cylindrical buildings, which are also of great practical interest. In contrast to rectangular buildings, these have the special feature that the separation point is not fixed but must be an outcome of the numerical calculation.

Cooling towers are an important example of round structures exposed to the wind. Although the wind loading and the development of the wind field near the tower are also of concern in this case, the greatest practical interest rests here with the plume spreading. For this, most practical calculations have so far been carried out with one-dimensional integral models (e.g. Schatzmann and Policastro [10]). These are rather simple and economical but they do not allow the simulation of any details of the flow field nor that of a number of important influences such as the downwash effect due to flow separation behind the tower, the bifurcation and associated horizontal flattening of the plume and the interaction with ground topography. Several 3-D field models have been developed for calculating plume spreading; in most of these, the originally elliptic equations have been simplified to parabolic ones in the wind direction so that they can be solved with economic numerical marching procedures. Such parabolic models are again not capable of simulating the complex flow in the direct vicinity of the tower where separation and bending-over of the plume occurs. Rather, the calculations start with profiles at an initial cross section above the tower, and these have to be prescribed with the aid of empirical input. When suitable profiles were chosen, realistic results could be obtained for a number of cases [11–14]. The flow in the direct vicinity of the tower can only be simulated by solving the original 3-D elliptic equations, which involves much higher computational cost. Because of this, only a few such calculations have been carried out. Both Crawford [15] and Pernecker [16] reported on some initial elliptic calculations, requiring much computing times in spite of using only very simple turbulence models which cannot do justice to the complex flow field considered. Recently, Demuren and Rodi [17] calculated the flow and plume

spreading past cylindrical model cooling towers for a number of parameter configurations using the k–ε turbulence model. They employed a rectangular grid so that the round tower shape had to be approximated by steps. This is certainly not a very suitable measure for resolving the boundary layer developing around the tower, but the separation induced (non-physically) by the steps roughly at the location of the maximum body width seems to be reasonable enough for the calculation of the rest of the flow field, as the most important features predicted agree reasonably well with measurements, such as the complex flow pattern behind the model tower and also the plume spreading. It is clear however that separation was not induced by the physically correct mechanism.

The present paper aims to show how well the flow and plume spreading past cylindrical structures can be predicted with a recently developed finite-volume method employing body-fitted curvilinear orthogonal grids and the same k–ε turbulence model used in other calculations mentioned. For this purpose, the 3-D finite-volume method to be described is applied to two test cases, for which experimental data are available for comparison from model studies in the laboratory. The first test case is the flow around a surface-mounted circular cylinder of height-to-diameter ratio 1.9 immersed in a simulated atmospheric boundary layer studied in a wind tunnel by Hölscher and Niemann [18, 19]. The second test case concerns Viollet's [12] experiment on a cylindrical cooling tower model placed in an oncoming boundary layer in a water tunnel. From this model tower, a non-buoyant, but tracer-marked jet was discharged at a velocity 1.67 times the cross-wind velocity.

2. MATHEMATICAL MODEL

2.1 Choice of coordinate system

The time-averaged flow around cylindrical structures is governed by a set of coupled 3-D partial differential equations representing the conservation of mass and momentum, together with a suitable turbulence model. For the numerical solution of these equations, the discretization of the flow domain should conform to its boundaries in such a way that the boundary conditions can be represented accurately. In recent years, powerful methods [20] have been developed for generating boundary-fitted numerical grids for solving the flow equations in domains with curvilinear boundaries. The choice of the coordinate system is entirely problem-dependent; curvilinear coordinate systems need not necessarily be orthogonal, but the use of orthogonal systems requires the minimum modification to existing solution procedures employing 3-D Cartesian coordinates.

For calculating the flow around cylindrical bodies, the cylindrical polar coordinate system, i.e. radial polar on cross-sectional planes and simple Cartesian along the height of the cylinder (Fig. 1) appears to be the best choice as far as the specification of boundary conditions on the cylinder wall is concerned. However, the specification of the conditions along the outer boundary is not straightforward because the freestream velocity is not in the direction of the grid lines. Furthermore, special care is to be taken in discretizing the convective terms of the momentum equations for the control volumes above the
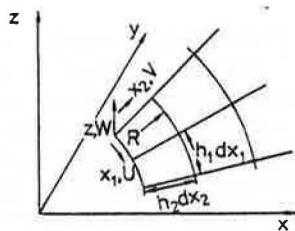
Fig. 1. Orthogonal curvilinear coordinate system.

cylinder top where the strong grid curvature relative to that of the flow tends to produce significant pressure errors [21]. Another disadvantage of the polar grid, particularly for simulating pollutant dispersion past structures, is that in the far region with nearly uniform velocity the grid of the symmetry plane is not aligned with the flow. This, together with the upwind discretization of convection terms, can lead to large numerical diffusion errors in solving the scalar transport equation. An alternative orthogonal grid system which allows the outer boundaries to be handled more conveniently is an H-grid composed of streamlines and potential lines for potential flow around cylinders where the inflow and outflow velocities are always in the direction of the coordinate lines. However, previous calculations of 2-D flow around cylinders performed by the authors [22] have shown that, compared to the cylindrical polar grid, the H-grid requires many more grid lines to obtain the same grid point concentration in the region near the cylinder wall and is therefore more expensive. Secondly, numerical inaccuracies are involved in the calculation of the cell curvature in an H-grid configuration whereas for the radial polar system the radii of curvature are precisely known. The present study concerns mainly the flow in the vicinity of cylindrical structures and therefore cylindrical polar coordinate systems are used in this work.

2.2 Mean-flow equations

The time-averaged differential equations governing the steady, 3-D turbulent flow and pollutant dispersion past cylindrical bodies may be written in the orthogonal curvilinear coordinate system (x_1, x_2, z) as follows.

Continuity:

$$\frac{1}{h_1 h_2}\left[\frac{\partial}{\partial x_1}(h_2 \rho U) + \frac{\partial}{\partial x_2}(h_1 \rho V) + \frac{\partial}{\partial z}(h_1 h_2 \rho W)\right] = 0. \tag{1}$$

Momentum along x_1:

$$\frac{1}{h_1 h_2}\left[\frac{\partial}{\partial x_1}(h_2 \rho U^2) + \frac{\partial}{\partial x_2}(h_1 \rho UV) + \frac{\partial}{\partial z}(h_1 h_2 \rho UW)\right]$$

$$= -\frac{1}{h_1}\frac{\partial P}{\partial x_1} + \frac{1}{h_1 h_2}\left[\frac{\partial}{\partial x_1}(h_2 \tau_{11}) + \frac{\partial}{\partial x_2}(h_1 \tau_{21})\right.$$

$$\left. + \frac{\partial}{\partial x_3}(h_1 h_2 \tau_{31})\right] + \frac{1}{h_1 h_2}\left[(\tau_{21} - \rho UV)\frac{\partial h_1}{\partial x_2}\right.$$

$$\left. - (\tau_{22} - \rho V^2)\frac{\partial h_2}{\partial x_1}\right]. \tag{2}$$

Momentum along x_2.

$$\frac{1}{h_1 h_2}\left[\frac{\partial}{\partial x_1}(h_2 \rho UV) + \frac{\partial}{\partial x_2}(h_1 \rho V^2) + \frac{\partial}{\partial z}(h_1 h_2 \rho VW)\right]$$

$$= -\frac{1}{h_2}\frac{\partial P}{\partial x_2} + \frac{1}{h_1 h_2}\left[\frac{\partial}{\partial x_1}(h_2 \tau_{12}) + \frac{\partial}{\partial x_2}(h_1 \tau_{22})\right.$$

$$\left. + \frac{\partial}{\partial x_3}(h_1 h_2 \tau_{32})\right] + \frac{1}{h_1 h_2}\left[(\tau_{12} - \rho UV)\frac{\partial h_2}{\partial x_1}\right.$$

$$\left. - (\tau_{11} - \rho U^2)\frac{\partial h_1}{\partial x_2}\right]. \tag{3}$$

Momentum along z:

$$\frac{1}{h_1 h_2}\left[\frac{\partial}{\partial x_1}(h_2 \rho UW) + \frac{\partial}{\partial x_2}(h_1 \rho VW) + \frac{\partial}{\partial z}(h_1 h_2 \rho W^2)\right]$$

$$= -\frac{\partial P}{\partial z} + \frac{1}{h_1 h_2}\left[\frac{\partial}{\partial x_1}(h_2 \tau_{13})\right.$$

$$\left. + \frac{\partial}{\partial x_2}(h_1 \tau_{23}) + \frac{\partial}{\partial x_3}(h_1 h_2 \tau_{33})\right]. \tag{4}$$

Passive Scalar ϕ:

$$\frac{1}{h_1 h_2}\left[\frac{\partial}{\partial x_1}(h_2 \rho U\phi) + \frac{\partial}{\partial x_2}(h_1 \rho V\phi) + \frac{\partial}{\partial x_3}(h_1 h_2 \rho W\phi)\right]$$

$$= \frac{1}{h_1 h_2}\left[\frac{\partial}{\partial x_1}(h_2 q_1) + \frac{\partial}{\partial x_2}(h_1 q_2) + \frac{\partial}{\partial z}(h_1 h_2 q_3)\right], \tag{5}$$

where the Reynolds stresses (τ) and turbulent scalar fluxes (q) are expressed as:

$$\tau_{11} = 2\frac{\mu_t}{h_1}\frac{\partial U}{\partial x_1} + 2\mu_t \frac{V}{h_1 h_2}\frac{\partial h_1}{\partial x_2},$$

$$\tau_{22} = 2\frac{\mu_t}{h_2}\frac{\partial V}{\partial x_2} + 2\mu_t \frac{U}{h_1 h_2}\frac{\partial h_2}{\partial x_1},$$

$$\tau_{33} = 2\mu_t \frac{\partial W}{\partial z},$$

$$\tau_{12} = \tau_{21} = \mu_t\left[\frac{h_1}{h_2}\frac{\partial}{\partial x_2}\left(\frac{U}{h_1}\right) + \frac{h_2}{h_1}\frac{\partial}{\partial x_1}\left(\frac{V}{h_2}\right)\right], \tag{6}$$

$$\tau_{23} = \tau_{32} = \mu_t\left[h_2 \frac{\partial}{\partial z}\left(\frac{V}{h_2}\right) + \frac{1}{h_2}\frac{\partial W}{\partial x_2}\right],$$

$$\tau_{31} = \tau_{13} = \mu_t\left[h_1 \frac{\partial}{\partial z}\left(\frac{U}{h_1}\right) + \frac{1}{h_1}\frac{\partial W}{\partial x_1}\right],$$

$$q_1 = \frac{\mu_t}{\sigma_\phi}\frac{1}{h_1}\frac{\partial \phi}{\partial x_1},$$

$$q_2 = \frac{\mu_t}{\sigma_\phi}\frac{1}{h_2}\frac{\partial \phi}{\partial x_2}, \tag{7}$$

$$q_3 = \frac{\mu_t}{\sigma_\phi}\frac{\partial \phi}{\partial z}.$$

The viscous stresses and molecular fluxes are neglected as the equations are not applied in this work to viscosity-affected near-wall regions which are bridged by wall functions as discussed in Section 2.5. The metric coefficients

are:

$$h_1 = \sqrt{\left(\frac{\partial x}{\partial x_1}\right)^2 + \left(\frac{\partial y}{\partial x_1}\right)^2} \quad \text{and}$$

$$h_2 = \sqrt{\left(\frac{\partial x}{\partial x_2}\right)^2 + \left(\frac{\partial y}{\partial x_2}\right)^2}. \quad (8)$$

Equations (1)–(5) reduce to the Cartesian equations by setting all metrics to unity. The metric coefficients h_1, h_2, however, always appear in the discretized equations either as cell dimensions $h_1 dx_1, h_2 dx_2$ (Fig. 1) or as the Christoffel symbols:

$$\frac{1}{h_1 h_2}\frac{\partial h_1}{\partial x_2} \quad \text{or} \quad \frac{1}{h_1 h_2}\frac{\partial h_2}{\partial x_1},$$

which are, in a physical sense, the curvature of the grid lines along the x_1 and x_2 directions. Explicit evaluation of the metric coefficients are therefore not needed when the finite cell dimensions and their curvatures are known. For the cylindrical polar coordinate system used in this study, the metric coefficients and the cell curvatures are:

$$h_1 = R; \quad h_2 = 1; \quad \frac{1}{h_1 h_2}\frac{\partial h_1}{\partial x_2} = \frac{1}{R}; \quad \frac{1}{h_1 h_2}\frac{\partial h_2}{\partial x_1} = 0.$$

2.3 Turbulence modelling

The use of an eddy viscosity implies of course a turbulence model assumption which relates the originally appearing Reynolds stresses to the gradients of time-averaged velocities and in a similar way the turbulent scalar fluxes to the gradients of the scalar quantity. The distribution of μ_t over the flow field has to be provided also by the turbulence model.

The k–ε model of turbulence described in detail by Launder and Spalding [23] is employed here. It has been applied successfully to calculate many different turbulent flows [24, 25]. This model calculates the eddy viscosity (μ_t) via the relation:

$$\mu_t = \rho c_\mu k^2/\varepsilon. \quad (9)$$

The spatial distribution of the turbulent kinetic energy k and its rate of dissipation ε are obtained by solving semi-empirical transport equations for these quantities, which may be written in the present curvilinear orthogonal coordinates as:

$$\frac{1}{h_1 h_2}\left[\frac{\partial}{\partial x_1}(h_2 \rho U k) + \frac{\partial}{\partial x_2}(h_1 \rho V k) + \frac{\partial}{\partial z}(h_1 h_2 \rho W k)\right]$$

$$= \frac{1}{h_1 h_2}\left[\frac{\partial}{\partial x_1}\left(\frac{h_2}{h_1}\frac{\mu_t}{\sigma_k}\frac{\partial k}{\partial x_1}\right) + \frac{\partial}{\partial x_2}\left(\frac{h_1}{h_2}\frac{\mu_t}{\sigma_k}\frac{\partial k}{\partial x_2}\right)\right.$$

$$\left. + \frac{\partial}{\partial z}\left(h_1 h_2 \frac{\mu_t}{\sigma_k}\frac{\partial k}{\partial z}\right)\right] + G - \rho\varepsilon, \quad (10)$$

$$\frac{1}{h_1 h_2}\left[\frac{\partial}{\partial x_1}(h_2 \rho U \varepsilon) + \frac{\partial}{\partial x_2}(h_1 \rho V \varepsilon) + \frac{\partial}{\partial z}(h_1 h_2 \rho W \varepsilon)\right]$$

$$= \frac{1}{h_1 h_2}\left[\frac{\partial}{\partial x_1}\left(\frac{h_2}{h_1}\frac{\mu_t}{\sigma_\varepsilon}\frac{\partial \varepsilon}{\partial x_1}\right) + \frac{\partial}{\partial x_2}\left(\frac{h_1}{h_2}\frac{\mu_t}{\sigma_\varepsilon}\frac{\partial \varepsilon}{\partial x_2}\right)\right.$$

$$\left. + \frac{\partial}{\partial z}\left(h_1 h_2 \frac{\mu_t}{\sigma_\varepsilon}\frac{\partial \varepsilon}{\partial z}\right)\right] + c_1 \frac{\varepsilon}{k}G - c_2 \rho\varepsilon^2/k, \quad (11)$$

where:

$$G = \mu_t\left[2\left(\frac{1}{h_1}\frac{\partial U}{\partial x_1} + \frac{V}{h_1 h_2}\frac{\partial h_1}{\partial x_2}\right)^2 + 2\left(\frac{1}{h_2}\frac{\partial V}{\partial x_2}\right.\right.$$

$$\left.+ \frac{U}{h_1 h_2}\frac{\partial h_2}{\partial x_1}\right)^2 + 2\left(\frac{\partial W}{\partial z}\right)^2 + \left(\frac{\partial V}{\partial z} + \frac{1}{h_2}\frac{\partial W}{\partial x_2}\right)^2$$

$$+ \left(\frac{\partial U}{\partial z} + \frac{1}{h_1}\frac{\partial W}{\partial x_1}\right)^2 + \left(\frac{1}{h_1}\frac{\partial V}{\partial x_1} + \frac{1}{h_2}\frac{\partial U}{\partial x_2}\right.$$

$$\left.\left.- \frac{V}{h_1 h_2}\frac{\partial h_2}{\partial x_1} - \frac{U}{h_1 h_2}\frac{\partial h_1}{\partial x_2}\right)^2\right]. \quad (12)$$

where, for the turbulence model constants in Equations (10) and (11) and for the turbulent Prandtl number (σ_ϕ), standard values are adopted from Rodi [24]: $c_\mu = 0.09$, $c_1 = 1.44$, $c_2 = 1.92$, $\sigma_k = 1.0$, $\sigma_\varepsilon = 1.3$ and $\sigma_\phi = 0.5$.

2.4 Finite-volume procedure

In a finite-volume method, the differential equations governing the flow are first integrated over finite control volumes covering the flow domain to frame the finite-volume equations as a set of coupled linear algebraic equations. As the basis of the development, the finite-volume procedure for calculating incompressible flows in 2- and 3-D Cartesian systems using the well known SIMPLE algorithm as described in [26] has been used. In an orthogonal curvilinear coordinate system, the discretized continuity and the passive scalar equations are direct generalisations of their Cartesian counterparts. On the other hand, the momentum equations and the turbulence production (G) contain additional coordinate-curvature terms which have no counterpart in the corresponding Cartesian equations. The discretization of the convective and diffusive terms of the equations to obtain the fluxes at the control-volume faces is quite similar to the discretization in the Cartesian system when appropriate lengths, areas and volumes are considered for the curved control volumes. The curvature terms are usually discretized as volume source terms irrespective of whether they are convective or diffusive terms in a physical sense.

The discrete approximation of the transport equations in general orthogonal coordinates introduces errors analogous to those found in Cartesian equations, mainly numerical diffusion errors from the upwind-difference discretization of the convective terms. However, calculations with curvilinear grids employing grid-aligned velocity components are reported [21] to suffer from another serious error, the so-called "false pressure error" due to the use of the conventional upwind approximation of the Cartesian system in the momentum equations for the convected velocity components which change direction from one control volume to another. The source of these errors, and remedies for reducing them to a minimum, were first discussed by Galpin *et al.* [21, 27]. Preliminary test calculations for a few simple 2-D flow situations carried out by the present authors have also confirmed the serious effect of the "false pressure error" on the solution, especially where the grid curvature is rather large compared to a relatively straight flow. The present finite-volume method therefore employs the

"streamline curvature-weighted vector differencing scheme" proposed by Galpin *et al.* [21, 27] to discretize the convected velocity components on the control volume faces in the U and V momentum equations. The details of how to evaluate the local weighting functions depending on the curvature of grid and streamlines at cell faces are described in [27]. Before applying this discretization method to the complex 3-D problem considered here, it was tested for 2-D uniform flow and potential free-vortex flow in a radial polar grid, where the exact analytical solutions are known.

The present method uses a staggered variable arrangement, grid-oriented velocity components, hybrid central/upwind discretization for the convective terms in general and the special streamline curvature weighted vector upstream differencing for the convected velocity components in the U and V momentum equations. The SIMPLEC algorithm proposed by Vandoormal and Raithby [28] is used to calculate the pressure field. This algorithm allows the use of high values of under-relaxation parameters for all variables (0.8 was used for the three velocities, 0.75 for scalars and 1.0 for pressure in the calculations reported) and consequently accelerates the convergence; it is basically a modified version of the algorithm SIMPLE [26] in which an iterative guess and correct procedure is employed to evaluate the pressure and velocity field in such a way that it simultaneously satisfies the mass continuity and the momentum conservation equations. During each iteration, the set of linear algebraic finite difference equations for each variable is solved sequentially using a line-iterative TDMA (Tri-Diagonal-Matrix Algorithm) procedure. Since good mass conservation is crucial at every outer iteration for efficient and reliable solution when an uncoupled procedure like SIMPLEC is used, a given percentage (10% for the present problems) of the initial residuum (continuity error) is prescribed as termination criterion of the pressure-correction sweep in each outer iteration for continuity. The calculations performed with the hybrid differencing scheme presented below are expected to suffer to some extent from errors due to numerical diffusion; but calculations using finer grids to reduce these errors were not possible with the computer available.

2.5 *Boundary conditions*

The mathematical model is applied to simulate the following two flow situations: (i) flow around a model cylinder immersed in a simulated atmospheric boundary layer; (ii) flow above and around a model cooling tower placed in a water tunnel. In both cases, the computational domain has the following boundaries: inflow surface, outflow surface, bottom wall of the test tunnel, surfaces of the cylinder or tower model, domain top (located far away from the cylinder) and midplane of the test set-ups (because of symmetry, only one half of the flow field needs to be calculated). In general, boundary conditions need to be specified for all dependent variables at all boundaries.

At the symmetry plane, the normal gradients of all the variables are set to zero except for the velocity normal to the plane which itself is zero. At the cylinder surfaces, at inside or outside surfaces of the tower and at the tunnel floor, the wall function procedure described in detail in Launder and Spalding [23] is employed. In this procedure, the viscous sublayer is bridged by relating the velocity components parallel to the wall and the value of k and ε at the first grid point (located outside of the viscous sublayer) to the resultant friction velocity. In particular, use is made of the "universal" logarithmic velocity distribution, and the assumption of local equilibrium between production and dissipation of turbulence. At all surfaces, the gradient of the passive scalar normal to the surface was set to zero.

3. MODEL APPLICATION

3.1 *Flow around surface-mounted circular cylinder*

Test case. The numerical model was applied to simulate a laboratory flow studied by Hölscher and Niemann [18, 19]. These authors placed a circular cylinder of height-to-depth ratio 1.9 on the floor of a wind tunnel on which an atmospheric boundary layer was simulated, and they determined the flow pattern on the floor and cylinder surfaces with an oil flow visualization technique (see Figs 5 and 7) and measured the pressure distribution around the cylinder. The wind tunnel cross section was 1.8 m wide and 1.6 m high, and the cylinder had a height of 0.6 m and a diameter of 0.315 m. Following Counihan [29], a thick boundary layer was generated by placing vortex generators 6.3 m upstream of the location of the cylinder and by covering the wind tunnel floor with distributed roughness elements (blocks of height 16 mm and 36 mm) for a length of 5.5 m. The rough floor ended 3 diameters upstream of the cylinder so that the floor was smooth in the vicinity and downstream of the cylinder. Boundary-layer characteristics in the absence of the cylinder were measured at the location where the cylinder was to be placed. The velocity was such that the Reynolds number based on the cylinder diameter and the velocity at the cylinder top was $Re = 5 \times 10^5$. The exponent of the boundary-layer velocity profile was found to be $\alpha = 0.185$. The thickness of the artificially generated boundary layer was 1.2 m so that the cylinder was totally immersed in the boundary layer. It should be mentioned that in [19] pressure measurements are reported for a cylinder with rib roughness, while the calculations were carried out assuming a smooth cylinder for which pressure measurements were only communicated by Hölscher [18].

Computational details. Figures 2a and b show the $45 \times 42 \times 40$ grid used for the calculation, illustrated on the vertical plane $x_1 = 0$ and the horizontal plane $z = 0$ respectively, along with the relevant boundary conditions. The storage capacity of the computer available did not allow the use of any finer grids. The grid was concentrated near the vertical cylinder surface in the x_2-direction and near the cylinder top as well as near the ground in the z-direction for better resolution of the near-wall regions with high gradients. Along the circumferential (x_1) direction, however, uniform grid spacing was used. The boundary layer developing on the cylinder wall was resolved by 10 grid points in the radial (x_2) direction just before the separation point. Using the above mentioned grid, the value of the dimensionless near-wall distance (y^+) could be kept below 200 on the cylinder top and near the rough ground at the floor,
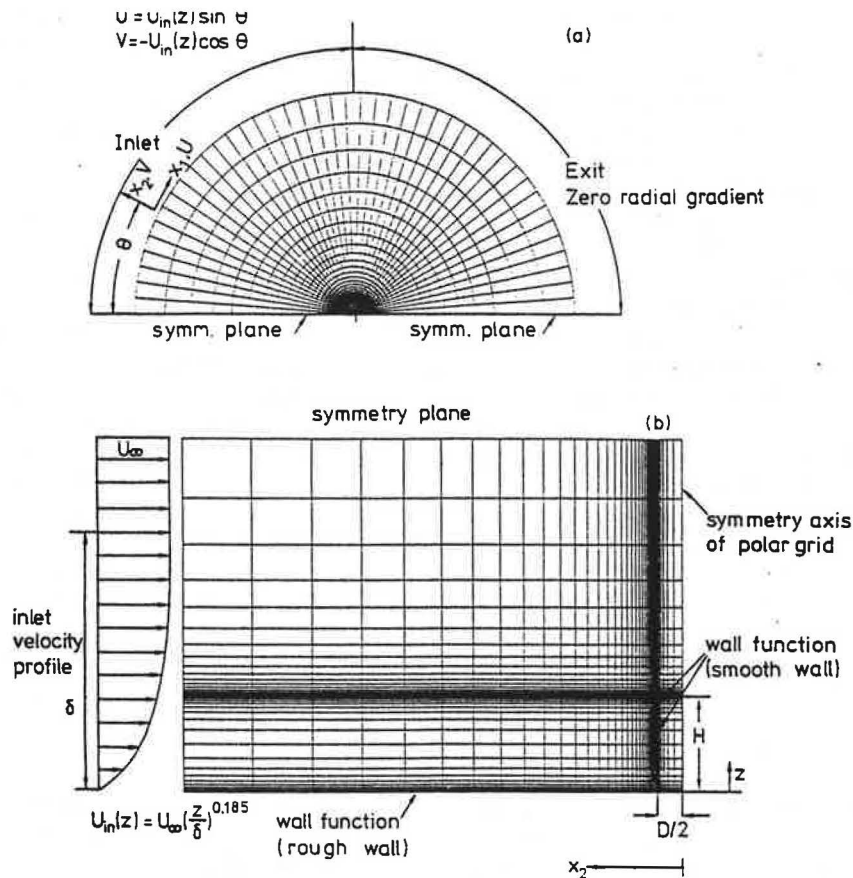
Fig. 2. Grid and boundary conditions for flow around surface-mounted cylinder: (a) on horizontal plane
($z = 0$); (b) on vertical plane ($x_1 = 0$).

whereas y^+ did not exceed 150 anywhere on the vertical cylinder surface. The average core storage required with this grid was approximately 8 megabytes using single precision arithmetic on a Siemens 7881 computer. Convergence was achieved in 60 iterations, requiring a total CPU time of about 2 h.

The measured velocity profile at the cylinder location of the tunnel without the cylinder has been used as the inlet velocity distribution for the calculation. Assuming that the profile does not change considerably in the downstream direction, the exponent $\alpha = 0.185$ from the measurements may be used to specify the inlet velocity. The velocity components U and V at the inlet along relevant directions (Fig. 2a) are then determined from the resolution of the resultant horizontal velocity $U_{\text{in}}(z)$. With the velocity profile known, the wall shear stress was calculated by matching a logarithmic law for rough walls to the specified power law profile at least for a few points near the wall. A comparison of logarithmic law and power law for the velocity gives:

$$U_{\text{in}}(z) = U_\infty \left(\frac{z}{\delta}\right)^\alpha = \frac{1}{\kappa} U_\tau \ln (z/z_s) + C, \qquad (13)$$

where z_s is the average geometrical roughness height and C is a constant depending on the roughness. Assuming as crude measure an average roughness height z_s of 10 mm for the whole ground covered by the calculation, the

values of U_τ and the constant C may be evaluated from the measured velocity profile using Equation (13). The kinetic energy of turbulence k and its dissipation rate ε at the first grid point near the ground were then calculated from the following relationship assuming local equilibrium between production and dissipation in this region:

$$k = \frac{U_\tau^2}{\sqrt{c_\mu}} \qquad \varepsilon = \frac{U_\tau^3}{\kappa z}. \qquad (14)$$

In the free stream ($z > \delta$) a low free-stream turbulence level ($k = 0.0025\ U_\infty^2$) and an eddy viscosity $\mu_t = 100 \times$ laminar viscosity was specified from which the free-stream value of ε follows as $\varepsilon = \rho c_\mu k^2/\mu_t$. For the other nodes inside the boundary layer, a linear distribution is assumed between the free-stream level and the near-wall values of k and ε. In the present calculation, the log law for rough walls was used for every point near the ground on which the cylinder stands, even though in the experiments the tunnel floor changed from a rough to a smooth wall at a plane 3 diameters upstream of the cylinder. The simulation of such a transition in roughness was difficult to introduce in the calculation for the following reasons: (i) with a radial polar grid it is difficult to incorporate the transition along a definite cross-sectional plane; (ii) some preliminary calculations have shown that removing the roughness in the log law applied to the flow

starting with the measured rough profile produces a far too quick return to a smooth wall boundary layer with relatively low turbulence while the artificially generated boundary layer in the experiment remembers much longer its previous history and only changes slowly. In order to keep up the high turbulence originating from the vortex generators and roughness elements, the rough wall law is used in the calculation assuming an average roughness height of $z_s = 10$ mm.

Model predictions. The calculated velocity vectors in the vertical symmetry plane are shown in Fig. 3. Upstream of the cylinder, the specified boundary-layer profile can be seen as well as the deceleration of the flow as it approaches the front stagnation line on the cylinder. If the cylinder were infinitely long and the approach flow were uniform, the flow would simply turn around the cylinder (in the way shown in Fig. 4). It is clear however from Fig. 3 that the approach flow turns upward in the upper half of the cylinder, which is due to the finite height of the cylinder; in the lower half, the approach flow turns downward because of the strong shear near the floor. The flow separates in the corner, forming a vortex which wraps itself around the cylinder to become the well-known horse-shoe vortex (see also Fig. 9). Near the top, the flow is lifted over the cylinder, separating at the leading edge but reattaching around the middle of the cylinder roof. This behaviour is in agreement with observations from surface flow patterns (Fig. 5), which indicate, however, the existence of a small counter-rotating vortex along the leading edge which is not resolved in the calculations. In the wake behind the cylinder, a very complex flow develops with reverse flow indicating separation which extends to roughly 0.8 diameters downstream of the cylinder near the floor. Again, an upward velocity component can be seen in the upper half of the cylinder height, which is associated with the streamwise vortex spinning off the roof edge. Near the floor, a downward velocity component exists which is due to the horse-

shoe vortex in the corner and basically acts to carry fluid into the sizeable reverse flow region near the floor. Beyond reattachment, the redevelopment of the boundary layer can be observed and also the deficit of the velocity in the wake of the cylinder over the free-stream velocity.

Figure 4 displays calculated velocity vectors in horizontal planes at various heights. Figure 4a shows the vectors at the first grid point from the floor ($z/H = 0.0036$) and hence gives an impression of the flow pattern very near the surface which may be compared, in certain respects, with the photograph in Fig. 5 showing the surface pattern obtained by the oil flow visualization technique in the wind tunnel. It can be seen from Fig. 4a that the separation upstream of the cylinder extends to about $0.7D$, which is somewhat more than the separation length of approximately $0.5D$ that can be interpreted from the visualization photograph. The outward movement of the flow away from the cylinder in the front part is very similar to that seen in the photograph in Fig. 5. Further around the cylinder, the flow can be seen to separate at $\theta = 95°$, which is somewhat earlier than indicated by the visualization picture (see also Fig. 7). In the region downstream of the separation point, the formation of a vertical vortex can be seen, which has some similarity to the strong vortex apparent in Fig. 5 (drilling vortex, white areas), but the latter is located significantly closer to the symmetry plane. Between this plane and the vertical vortex in the calculations an outward flow is present, which is due to the horse-shoe vortex as can be seen clearly from Fig. 9b. This outward flow appears not to be present in the experiments, indicating that no horse-shoe vortex existed in this region as it probably separated from the cylinder and was diffused. The flow picture shown in the photograph of Fig. 5 is in fact closer to the calculated flow pattern higher up at $z/H = 0.43$, but having a larger separation zone.

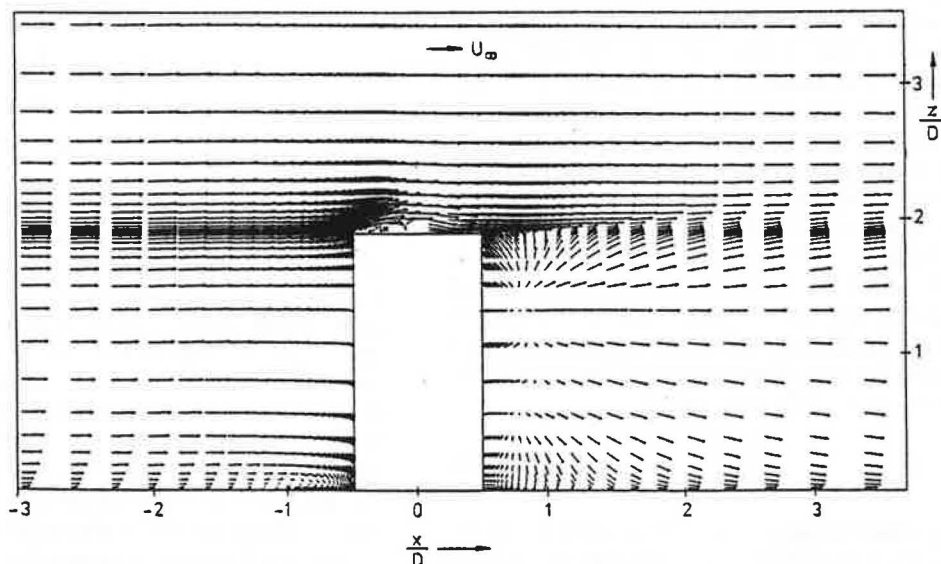The development of the flow near the floor and in

Fig. 3. Calculated velocity vectors on the vertical plane of symmetry for flow around surface-mounted cylinder.
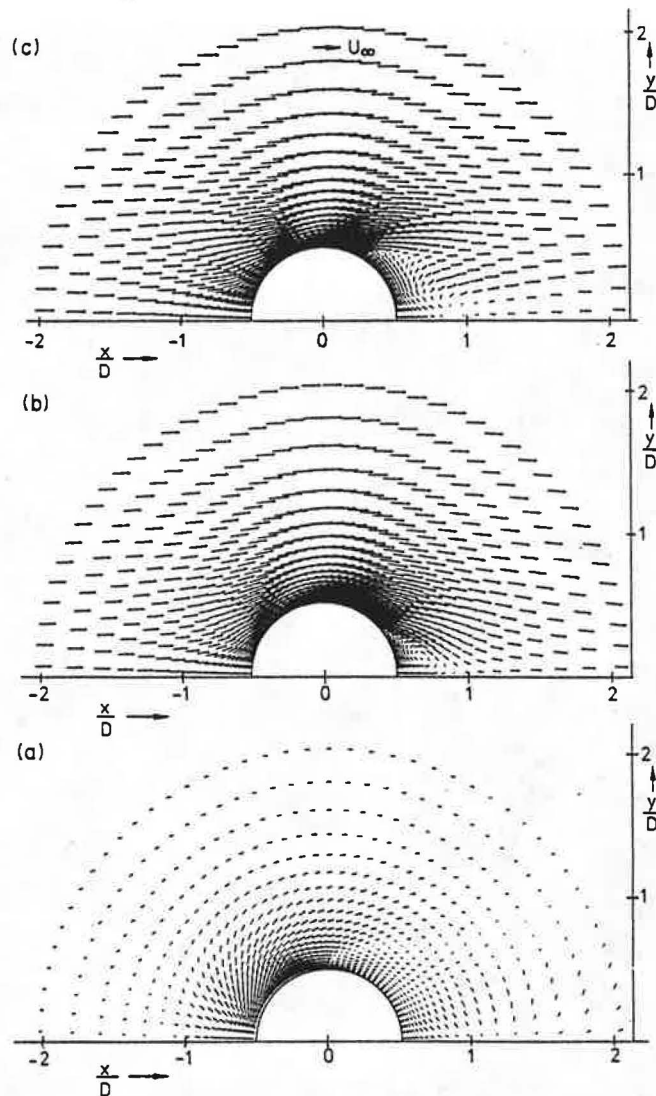
Fig. 4. Calculated velocity vectors in horizontal planes at various heights for flow around surface-mounted
cylinder: (a) $z/H = 0.0036$; (b) $z/H = 0.43$; (c) $z/H = 0.96$.

particular the formation and decay of the horse-shoe vortex are very sensitive to the characteristics of the oncoming boundary layer. The differences between the calculated and observed behaviour are mainly due to the fact that the boundary layer development in the experiments, in which a change in surface roughness was present, could not be reproduced accurately in the calculations, leading to the formation of an excessively strong horse-shoe vortex. It is interesting to note that in the cooling tower calculations, in which a different boundary layer profile was prescribed, the flow picture near the ground surface (Fig. 14a) is much more similar to the one apparent from the visualization picture in Fig. 5, both with respect to the separation ahead and behind the cylinder. The location of the vertical vortex is closer to the symmetry plane, there is no outward motion and hence no horse-shoe vortex in the separated flow region, and the general flow picture can be seen to concur closely with that in Fig. 5. It should further be mentioned that more grid points are probably needed in the near-floor

region in order to do justice to the very complex flow behaviour there.

Higher above the floor, where the oncoming boundary layer has much less influence, the flow around the cylinder is close to 2-D flow (Fig. 4b. $z/H = 0.43$). Separation takes place now much later at $\theta \approx 140°$, which is somewhat later than in the experiment. This disagreement is probably due to the k–ε turbulence model, which is known to perform rather poorly in calculating decelerating boundary layers and tends to produce late separation. Figure 4b further shows that the separation zone is rather short, but no experimental information is available to assess whether this is realistic.

When the top of the tower is approached, separation again occurs earlier (Fig. 4c, $z/H = 0.96$). This shift of the separation location is associated with the upward motion in this region and the formation of the streamwise vortex spinning off the roof edge (see Fig. 9b). It is clear from Fig. 7 showing the flow pattern on the rear of the cylinder from the visualization experiments that the
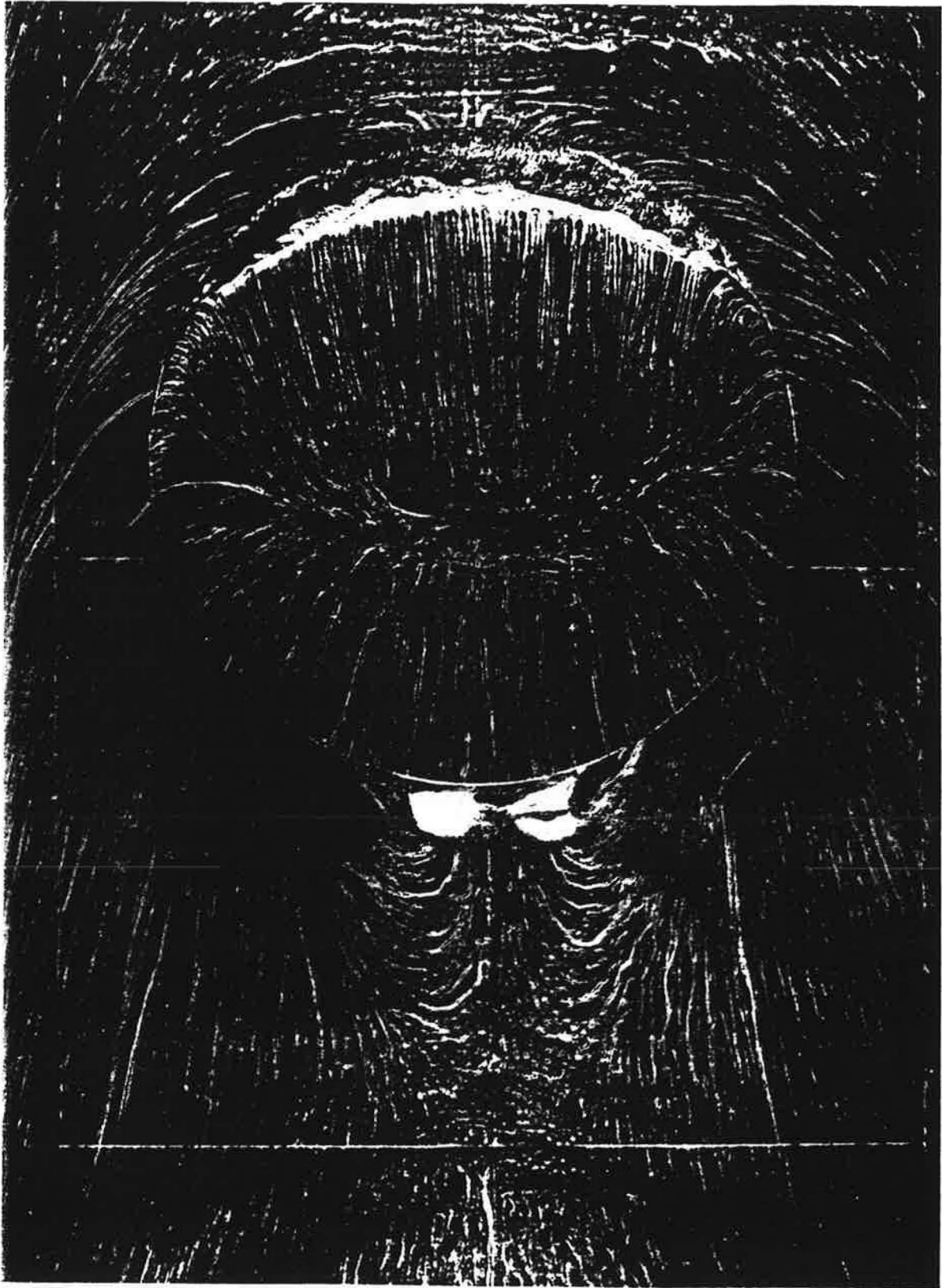
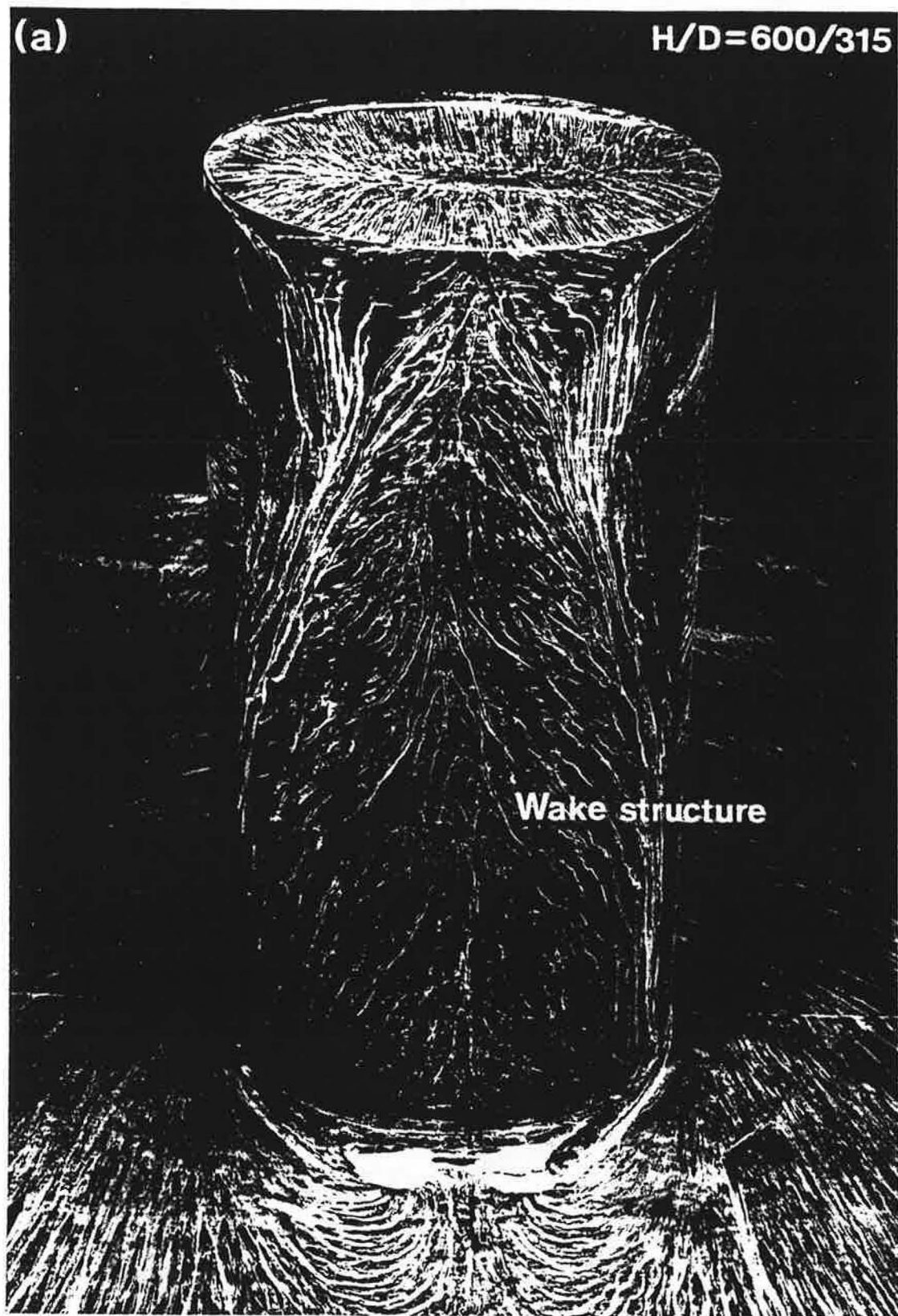Fig. 5. Surface flow visualization photograph viewed from top of the surface-mounted cylinder [18].

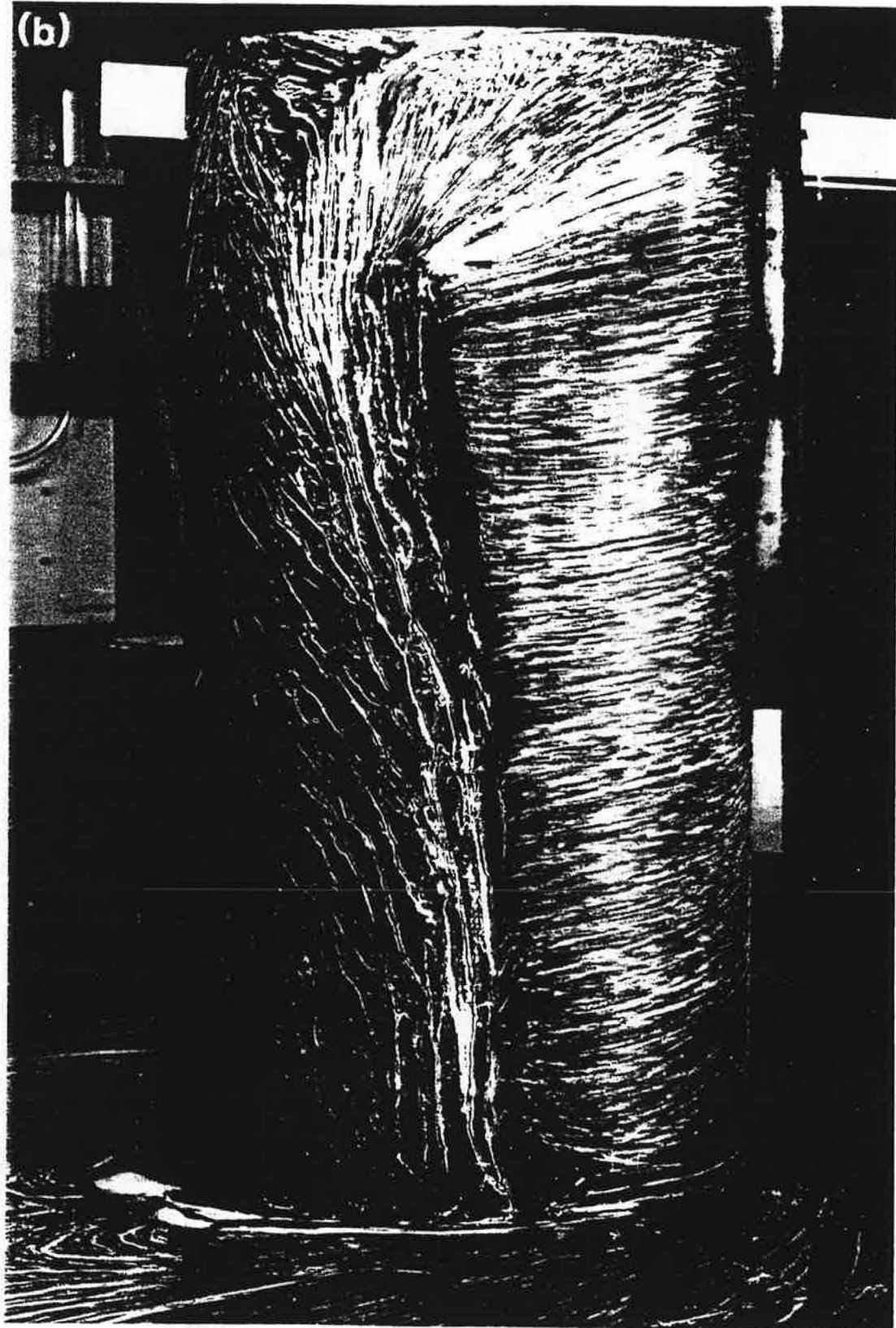Fig. 7. Surface flow visualization photographs [18] : (a) rear view ; (b) side view.

Fig. 7—*continued.*

separation line does indeed move forward very near the cylinder top. Figure 6 summarizes the separation behaviour by giving the predicted variation of the separation location with height. This predicted separation line can be compared qualitatively with the separation line apparent from the surface flow visualization pictures in Fig. 7. There is quite close general agreement, i.e. the separation zone in the upper part first narrows and then widens strongly as the top is approached, and near the floor the separation line also moves considerably upstream (see Fig. 7b). However, because the horse-shoe vortex is predicted too strong, the separation line turns upstream too high above the floor in the calculations.

In Fig. 8, the calculated velocity vectors are shown in the horizontal plane at the first grid point above the cylinder roof ($z/H = 1.0035$). In order to avoid confusion and to allow a direct comparison with the surface pattern from the flow visualization study shown in Fig. 5, the vectors are shown only for the cylinder area. The flow separates at the leading edge, but at the plane shown, which is somewhat above the roof, the velocity vectors for the first two grid points downstream from the leading edge are actually in the downstream direction. Reverse flow occurs over the front part of the roof, while over the rear part the flow is attached. However, away from the symmetry line, the calculated flow is much more radial than is indicated by the observed surface pattern. This may be due to the fact that the numerical grid in the radial direction is really too coarse for an adequate resolution of the flow over the cylinder top.

Figure 9 displays the calculated velocity vectors at the two downstream cross sections $x/D = 1$ and $x/D = 3$. The secondary velocities in these planes are rather small as can be seen by comparison with the free-stream velocity U_∞ also given in the figure. Near the floor and the symmetry plane, a longitudinal vortex is present as was discussed already, which appears to originate from the horse-shoe vortex. This vortex gets flattened in the downstream direction and then disappears. As discussed already, there is no indication that such a vortex exists in the experiments and hence it must be considered as unrealistic. Near the cylinder top, a further longitudinal
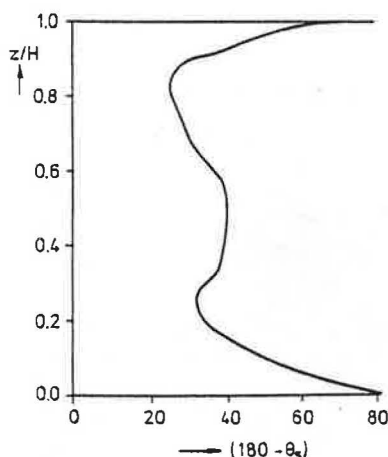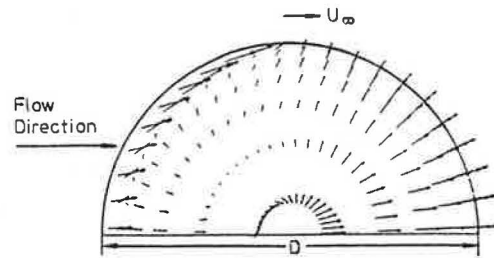

Fig. 8. Calculated velocity vectors near the roof of the surface-mounted cylinder ($z/H = 1.0035$).

vortex with clockwise rotation has evolved which is realistic. It originates from the vorticity of the boundary layer along the vertical cylinder walls and from the vertical vortex in the separated flow regions which are bent over into the streamwise direction by the flow over the cylinder roof. However, this vortex is not very strong and decays quickly in the downstream direction.

Figure 10 compares the predicted and measured pressure distributions around the cylinder at three different heights. The quantity plotted is the pressure coefficient C_p defined in Fig. 10, in which the local pressure is related to the pressure and velocity values at the same height in the undisturbed boundary layer flow upstream. At all heights, the pressure assumes a maximum value at the stagnation line; it then drops as the flow is accelerated around the front part of the cylinder. A pressure minimum is reached near $\theta = 90°$ beyond which the pressure rises again leading to separation of the boundary layer. After separation, the pressure levels off to the base pressure. The stagnation pressure is well predicted at all heights, and so is the pressure development in the accelerating flow region around the front part of the cylinder. The stagnation pressure increases as one moves from the top to the bottom of the cylinder; at mid-height the coefficient has a typical value of ≈ 1 as in 2-D flow. Near the bottom, the stagnation pressure increases due to the vortex generated there. The pressure minimum is also reasonably well predicted, but the following increase is not so accurately reproduced as separation is predicted too early near the bottom and somewhat too late in the middle portion. Apart from the bottom region, the base pressure in the calculations is not nearly as constant as in the experiments and is also considerably higher. A similar discrepancy was observed by Majumdar and Rodi [23] in their calculations of 2-D flow around a circular cylinder. The conclusion reached in that study was that the predicted base pressure was high because a steady calculation procedure was used in which any effects of vortex shedding were neglected. According to the study of Sakamoto and Arie [2], periodic vortex shedding with a preferred frequency also occurs for finite-height cylinders whose height-to-diameter ratio is above 1.5. The standard $k-\varepsilon$ model cannot handle this phenomenon and unsteady calculations resolving the periodic vortex shedding would really be necessary. On the other hand, the base pressure very near the floor is predicted too low, which is likely to be due to the fact that the flow field in this region was not accurately reproduced, as was discussed already.

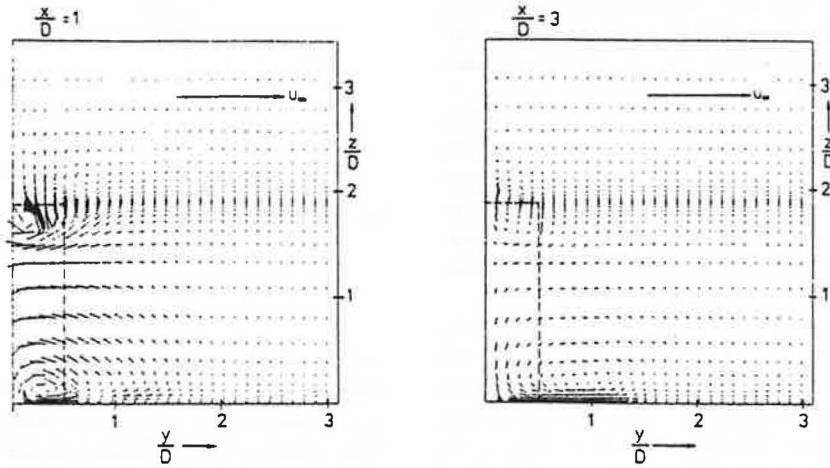Fig. 6. Variation of separation location along the height of the surface-mounted cylinder.

Fig. 9. Calculated velocity vectors in vertical cross-sectional planes for flow around surface-mounted cylinder.

Figure 11 compares calculated and measured lines of constant pressure coefficient C_p on the cylinder roof. Because of the very poor numerical resolution in the centre part, details of the pressure distribution in this area could not be obtained from the calculations and were hence extrapolated from the distribution in the outer part by dashed lines. On the upwind part of the roof, there is fairly close agreement between the calculated and the measured distribution, whereas towards the trailing edge the agreement is not so good as the calculated pressure is too high in this region, which was to be expected from the distribution of C_p in the separated region at $z/H = 0.95$ shown in Fig. 10. Because of this high pressure, the constant pressure lines do not close in the rear part of the roof as they do in the experiment.

3.2 Flow and plume spreading past a model cooling tower

Test case. The second test case to which the math-

ematical model was applied was the flow around a cylindrical cooling tower model investigated in a water tunnel by Viollet [12]. The height-to-diameter ratio of the cylindrical tower model was 1.64, and the model was placed on the floor of the water tunnel on which a boundary layer had developed whose thickness δ was 1.5 times the tower height. Viollet [12] does not mention whether any special measures were taken to generate the boundary layer, but he provided a measured velocity profile from which an exponent $\alpha = 0.196$ could be evaluated. The jet exiting from the tower top was seeded with an inert tracer whose dispersion downstream of the tower was determined by concentration measurements. Viollet carried out measurements for various parameter situations, but detailed measurements of the velocity and tracer concentration field are only reported for one particular situation, in which the Reynolds number (based on tower diameter and velocity at the tower top) was
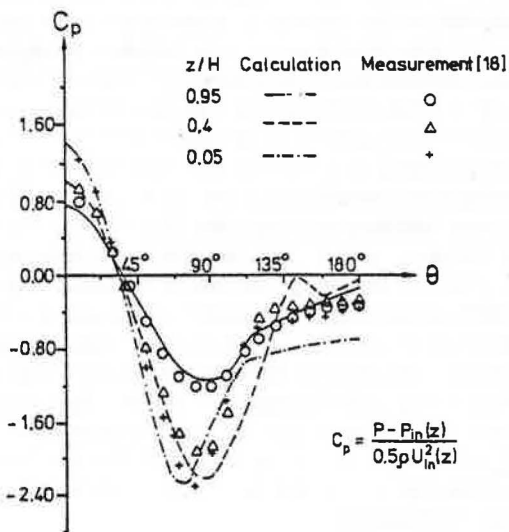

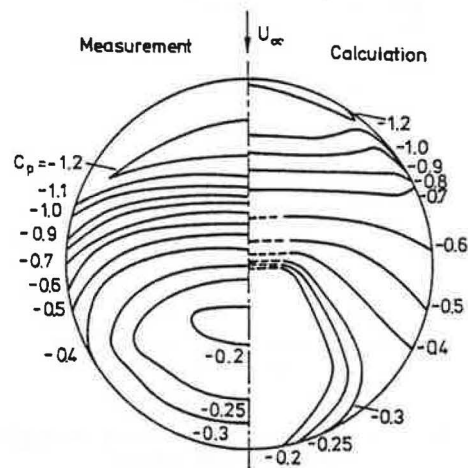Fig. 10. Pressure distribution around surface-mounted cylinder at various heights.

Fig. 11. Pressure distribution on the roof of the surface-mounted cylinder.

$Re = 2.57 \times 10^4$, the plume exit velocity was 1.67 times the cross flow velocity at the tower top, and there were insignificant density differences between the plume (actually a jet) and the cross flow so that buoyancy effects were virtually absent. This situation was taken as test case for the application of the mathematical model. For a different parameter situation, Viollet studied the influence of the Reynolds number on the dilution along the plume centre-line. He observed that this influence is small once the Reynolds number is above 2×10^4 so that the test case can be considered typical for large Reynolds number flow.

Computational details. Figures 12a and b show the grid and boundary conditions used for the calculation of flow around the model tower. The computation domain included both the inside and outside regions of the tower and therefore both outside and inside tower walls were within the computation domain. The radial polar grid used on the x_1–x_2 plane was the same as that in the cylinder case (described in Section 3.1) but since there was no wall at the top of the tower, the minimum grid spacing along z in the vicinity of the tower top was not limited by the requirements of the logarithmic law of wall. Uniform spacing equal to 0.1 times the tower height was used along the z-direction over a wide region near the tower top. The grid lines near the tower surface or the ground were again concentrated so that the value of

y^+ at the first grid point away from the wall did not exceed 100 anywhere in the field. The relevant components of the measured power law velocity profile at the inlet boundary around the outer periphery of the computation domain were prescribed in a manner similar to that for the cylinder test case. However, the tunnel floor was assumed to be smooth and the wall shear stress was determined by matching the power law profile to the following logarithmic law for smooth walls:

$$U_{in}(z) = U_\infty \left(\frac{z}{\delta}\right)^\alpha = \frac{1}{\kappa} U_\tau \ln\left(\frac{zU_\tau}{\nu} E\right). \quad (15)$$

Once the wall shear stress U_τ was determined, the near-wall values of k and ε were calculated using Equation (14), and the corresponding inlet profiles of the turbulence quantities were specified following the same procedure described for the cylinder test case in 3.1. At the bottom of the tower, uniform values of velocity (W), k and ε were prescribed for the flow inside the tower as follows: $W = 1.67 U_{in}(z = H)$, $k = 0.001 W^2$ and $\varepsilon = k^{3/2}/0.5D$. The requirements of computer storage and CPU time were approximately the same as for the cylinder test case.

Model predictions. The calculated and measured velocity vectors and iso-concentration lines are shown for the vertical symmetry plane in Fig. 13. The flow behav-
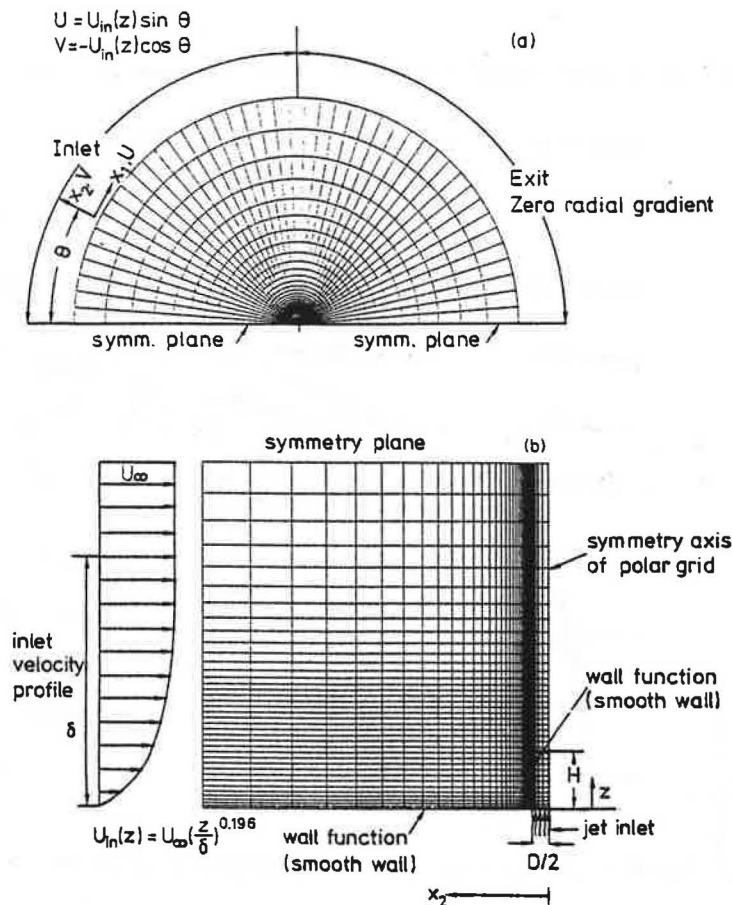

Fig. 12. Grid and boundary conditions for flow past model cooling tower: (a) on horizontal plane ($z = 0$); (b) on vertical plane ($x_1 = 0$).
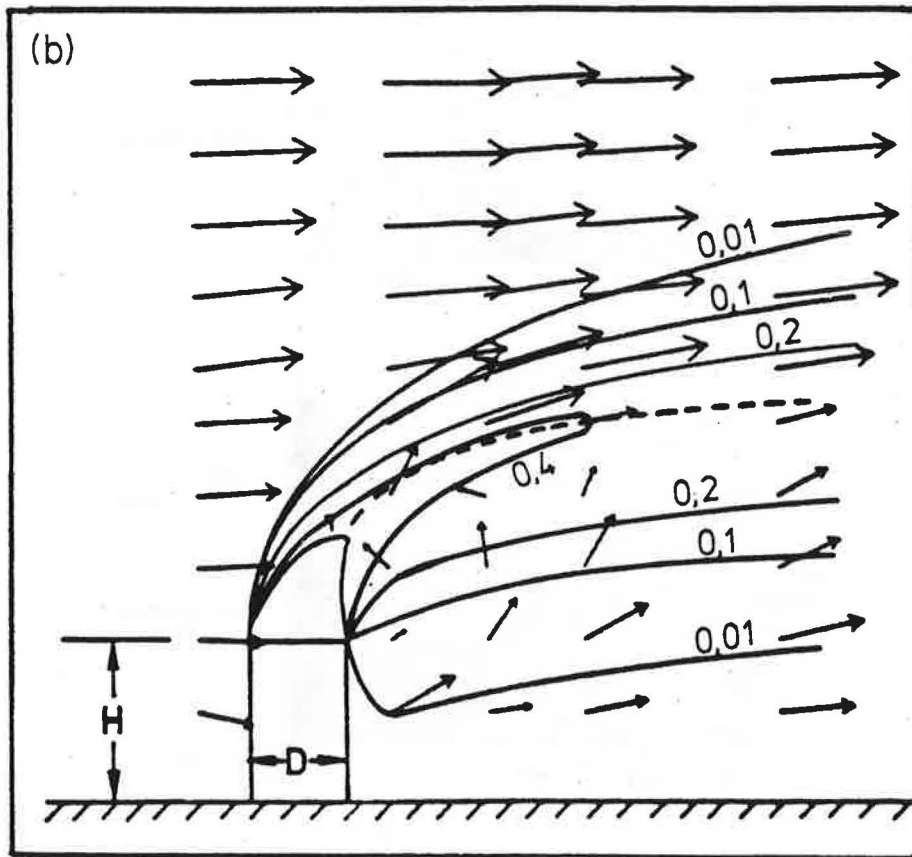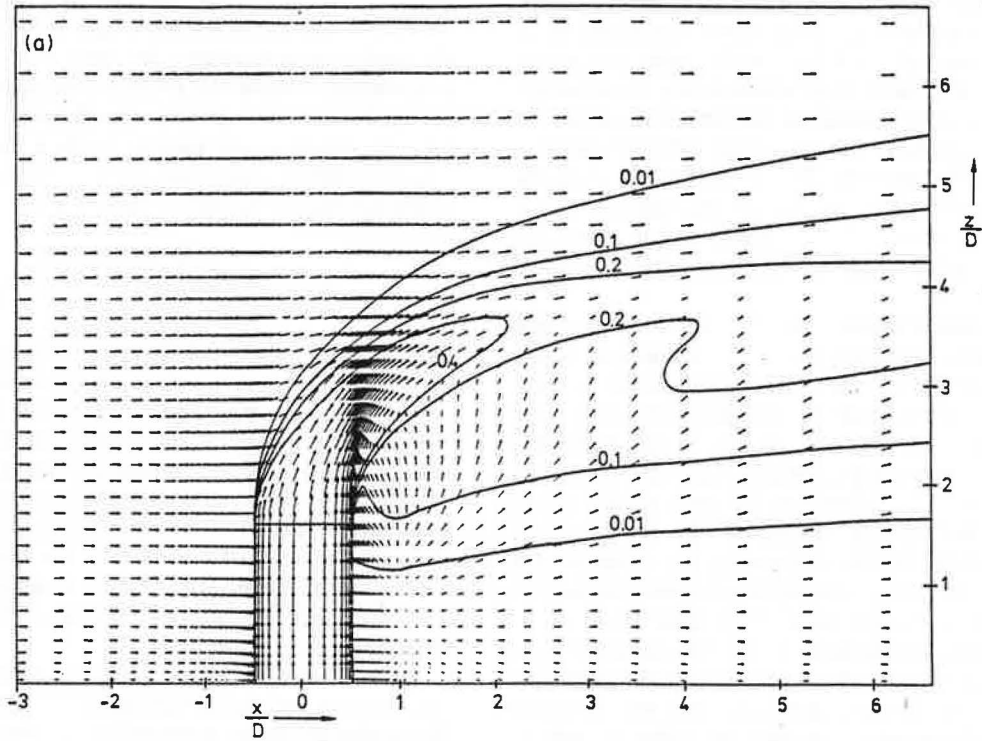
Fig. 13. Velocity vectors and iso-concentration lines in the vertical plane of symmetry for flow past model cooling tower: (a) calculation; (b) measurements.
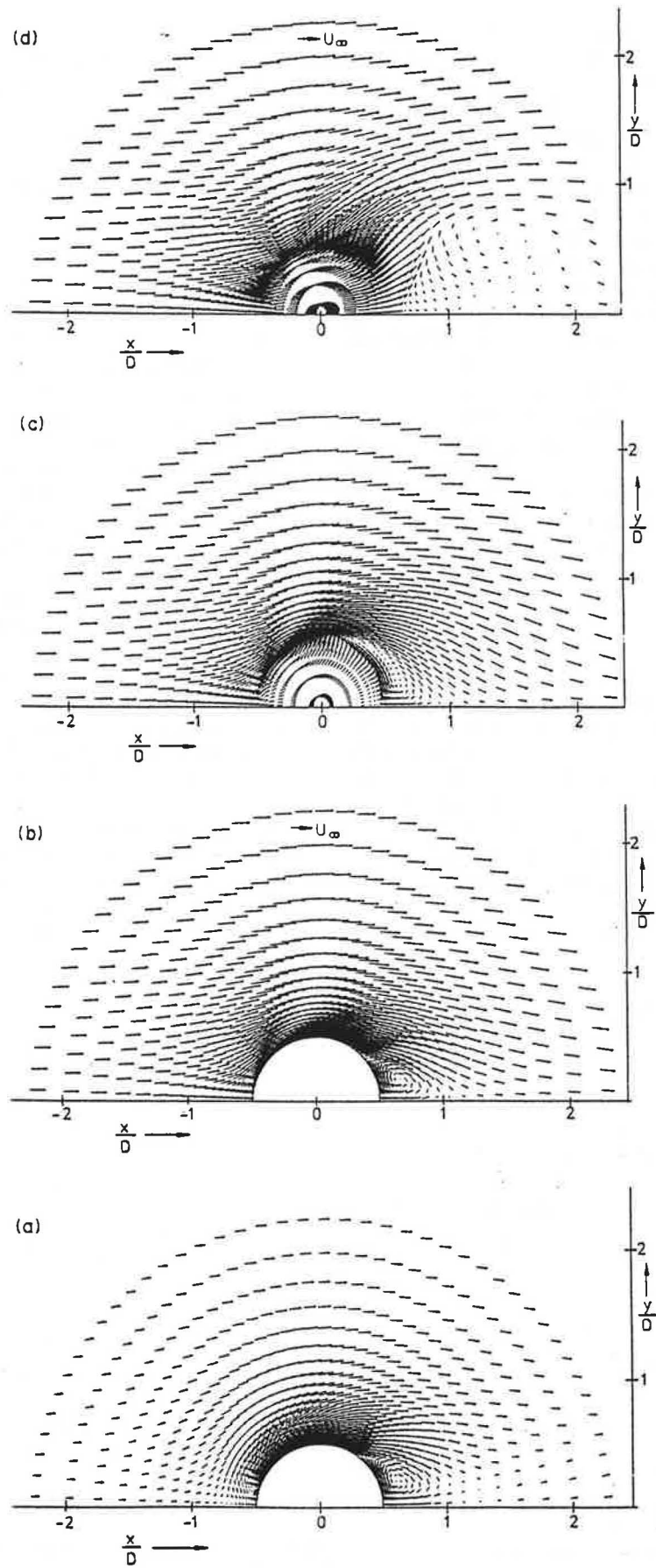
Fig. 14. Calculated velocity vectors in horizontal planes at various heights for flow past model cooling tower: (a) $z/H = 0.0226$; (b) $z/H = 0.45$; (c) $z/H = 1.05$; (d) $z/H = 1.45$.

iour upstream of the tower is very. similar to the one displayed in Fig. 3 for the cylinder case. Above the tower exit, the flow is dominated by the initially vertical jet which is bent over by the cross flow. Downstream of the tower, the flow shows a number of differences to the behaviour seen in Fig. 3 for the cylinder case. Firstly, there is a strong interaction of the flow around the tower with the bending-over jet, which entrains fluid, thereby causing an upward motion over a fairly large region. Further downstream, the upward motion is also due to the "filling-up" of the wake behind the bending-over jet, and it is strengthened by the longitudinal vortex generated by this jet as shown in Fig. 15. As opposed to the flow pattern shown in Fig. 3 for the cylinder, there is now hardly any downward motion near the floor behind the tower and hence also no horse-shoe vortex (see also Fig. 15a). In fact, the reverse flow behind the tower is essentially horizontal in the lower half of the tower height. This difference in flow behaviour near the floor is not due to the discharge of a jet at the top in the case of the tower model but due to differences in the oncoming boundary layer. The velocity vectors show that reverse flow does not occur only behind the tower itself, but also behind the bending-over jet, which also acts like an obstacle. It should further be mentioned that the fluid moving backward and upward behind the tower and the jet at the centre plane is provided by inflow from the side, as can be seen from the velocity vectors in Fig. 14. Comparing the calculated velocity vectors with the measured ones in Fig. 13b, close similarity can be observed, even though there may not be agreement in all details. Most of the features just discussed can also be observed from the measured velocity vectors. Unfortunately, however, the measurements did not extend close to the tower and to the floor.

The iso-concentration lines are also in general agreement; only the 0.2 line shows a somewhat erratic behaviour on the lower side at $x/D \approx 4$. It appears that an intrusion of low-concentration fluid occurs due to the upward velocity in this region, but this behaviour is unrealistic and is likely to be due to the relatively coarse polar

cylindrical grid employed. This problem was absent in the calculations of Demuren and Rodi [17] employing a rectangular grid, which was closely aligned with the flow direction in this downstream region. The 0.1 iso-concentration line indicates a similar intrusion near the trailing edge of the tower which in this case appears physically plausible because of the air entrainment from the ambient in this region.

Figure 14 presents the calculated velocity vectors in various horizontal planes, showing the flow around the cylindrical tower. Figure 14a portrays the flow in a plane at the first grid point away from the floor. The upstream separation can be seen to extend in this case only up to $\approx 0.2D$, indicating a much weaker horse-shoe vortex than in the cylinder case, and separation occurs at $\theta \approx 135°$. As was mentioned already, the predicted flow pattern near the floor has great similarity with the observed surface pattern near a cylinder shown in Fig. 5. At greater heights above the floor (Fig. 14b for $z/H = 0.45$), the pattern is very similar to the one near the floor, except that there is of course no separation upstream of the tower. In particular, the location of separation does not change significantly, which is consistent with the absence of a significant horse-shoe vortex. Near the tower top, the separation point also moves upstream in this case, as can be seen from Fig. 14c showing the velocity vectors at a plane just above the tower exit. Finally, Fig. 14d shows that a much larger separation region develops behind the bending-over jet which is located further downstream.

As is well known, the bending-over of rolled-up vortex sheets at the lee of jets in a cross flow leads to longitudinal vortices which persist quite a way downstream from the jet discharge. Fig. 15 displays calculated velocity vectors in cross-sectional planes at various distances from the tower, illustrating the longitudinal vortex, its lifting with the jet and its decay. By comparison with Fig. 9, it can be seen that a much stronger longitudinal vortex, which also persists much further downstream, is generated in this case than in the cylinder situation. The secondary motion of this vortex causes a distortion of the iso-concentration lines to kidney shape, which can be seen from
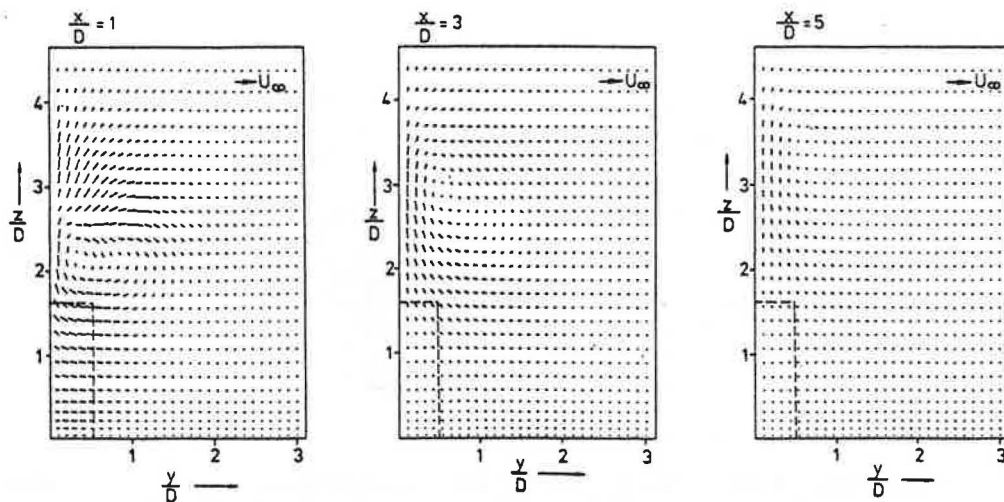

Fig. 15. Calculated velocity vectors in vertical cross-sectional plane for flow past model cooling tower.
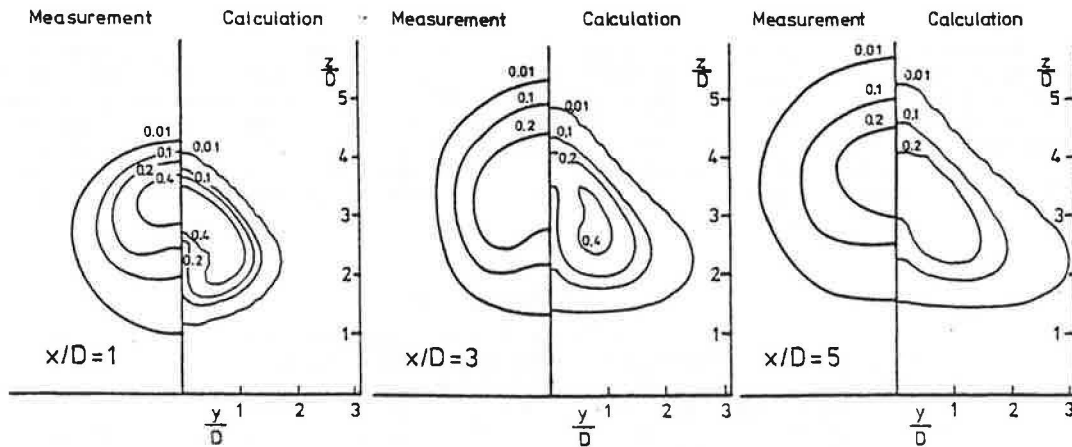
Fig. 16. Iso-concentration lines in vertical cross-sectional plane for flow past model cooling tower.

Fig. 16. It appears, however, that this distortion is excessive in the calculation and the shape of the lines becomes more and more triangular in the downstream direction while the measured shape is nearly round. Apparently, the behaviour is dominated by convection through the secondary motion and also by numerical diffusion acting in the wrong direction. With the upwind discretization scheme used, numerical diffusion must be expected to be fairly large in solving the concentration equation in the downstream region where the polar grid is rather coarse and at the same time increasingly skewed with respect to the streamlines as one moves away from the symmetry plane. This grid is therefore not very suitable for simulating the pollutant spreading in this region. Demuren and Rodi [17] obtained a much rounder shape of the iso-concentration lines and better agreement with the measurements using a rectangular grid aligned with the main flow direction.

4. CONCLUSIONS

A 3-D finite-volume method was presented for calculating the flow and plume spreading past surface-mounted cylindrical structures. It employs an orthogonal cylindrical-polar body-fitted numerical grid and the standard k–ε turbulence model with wall functions for bridging the viscous sub-layer. The application of the method to the flow around a circular cylinder and a cooling tower model has shown that many of the very complex flow features in the vicinity of circular structures immersed in a boundary layer could be simulated realistically. These features include the formation of the horse-shoe vortex, the separation behind the structure and in particular the separation line on the cylinder, the separation on the roof, the formation of vertical and longitudinal vortex systems, the interaction of the bending-over jet in the case of the cooling tower model with the flow around the tower, and the general pressure distribution on the cylinder surface. The flow development near the ground was found to be very sensitive to the near-wall characteristics of the oncoming boundary layer and to the boundary conditions prescribed on the ground which determine the further development of the boundary layer.

A rather crude treatment was employed for the experimental situation with a change-over from a rough ground to a smooth one, which is not fully satisfactory. This has led to the generation of an excessively strong horse-shoe vortex and, as a consequence, to a not entirely realistic flow very near the ground in the lee of the cylinder. More effort has to be spent on achieving an improved simulation of the boundary development near the ground. Also, more grid points are really needed to resolve this region with particularly complex flow pattern. The same is true for the region above the roof which could not be resolved adequately with the available computer allowing a maximum number of about 80,000 grid points. Future calculations should be carried out on a computer with a larger memory. The base pressure was generally calculated too high, resulting in an underprediction of the drag of the cylindrical structure. This is probably due to the fact that a steady calculation procedure was used which could not account for any vortex shedding that may have taken place in the experiments according to the earlier study of Arie and Sakamoto [2]. Unsteady calculations are called for to resolve the periodic unsteadiness, and the development of unsteady procedures has been started by calculating vortex shedding past two-dimensional cylinders [30]. However, already for two-dimensional problems the computing times are rather large. A considerably more powerful computer would be needed to extend the simulations to three dimensions. The plume spreading has been simulated fairly accurately in the vertical direction, while the calculation of the horizontal spreading appears to be spoiled somewhat by numerical diffusion errors. Off the symmetry plane, the polar grid lines are not aligned with the flow direction, which, together with the use of upstream differencing and a fairly coarse polar grid in the downstream region, must be expected to introduce serious numerical diffusion errors. Plume spreading calculations should therefore in future be carried out with a more suitable H-grid. It should be emphasized, however, that the calculated velocity field is much less affected by numerical diffusion errors because in the problematic downstream region the flow has become already fairly uniform.

REFERENCES

1. J. C. R. Hunt, C. J. Abell and J. A. Peterka, Kinematical studies of the flows around free or surface-mounted obstacles: applying topology to flow-visualization. *J. Fluid Mech.* **86**, 179–200 (1978).
2. H. Sakamoto and M. Arie, Vortex shedding from a rectangular prism and a circular cylinder placed vertically in a turbulent boundary layer. *J. Fluid Mech.* **126**, 147–165 (1983).
3. D. Vasilic-Melling. Three-dimensional turbulent flow past rectangular bluff bodies. Ph.D. thesis, University of London (1977).
4. I. P. Castro and A. G. Robins, The flow around a surface-mounted cube in uniform and turbulent streams. *J. Fluid Mech.* **79**, 307–335 (1977).
5. R. W. Benodekar, A. J. H. Goddard and A. D. Gosman, Predicting lift-off of major self-heating releases under the influence of a building. Rept. No. SR/016-(UK(N)-Project 3C). Imperial College, Mechanical Engineering Department (1983).
6. D. A. Paterson and C. J. Apelt, Computation of wind flow over buildings. *J. Wind Engng Ind. Aerodyn.* **24**, 193 (1986).
7. F. Baetke, Numerische Berechnung der turbulenten Umströmung eines kubischen Körpers. Ph.D. thesis, Technical University of Munich (1986).
8. F. Baetke, H. Werner and H. Wengle, Computation of turbulent flow around a cube on a vector computer. Proceedings of the 6th Symposium on Turbulent Shear Flows, Toulouse, France, 7–9 September (1987).
9. S. Murakami, A. Mochida and K. Hibi, Numerical simulation of air flow around cubic model. Proceedings of the International Symposium on Computational Fluid Dynamics. Tokyo, Japan, 9–12 September (1985).
10. M. Schatzmann and A. J. Policastro, An advanced integral model for cooling tower plume dispersion. *Atmosph. Envir.* **18**, 663–674 (1984).
11. J. P. Benqué, L. Caudron and P. L. Viollet, Modèle tridimensionnel de calcul de panaches émis dans l'atmosphère. Société Hydrotechnique de France, XIVes Journées de l'Hydraulique, Question V, Rapport 1, Paris (1976).
12. P. L. Viollet, Etude de jets dans des courants transversiers et dans des milieux stratifiés. Dissertation, Université Pierre et Marie Curie, Paris (1977).
13. W. Egler and G. Ernst, Dreidimensionales Ausbreitungsmodell für Kühlturmschwaden. Fortschrittberichte VDI, Reihe 15 (1979).
14. G. Schnabel, Mathematische Modellierung der Ausbreitung von Kühlturmschwaden mit zugemischten Rauchgasen. Fortschrittberichte VDI, Reihe 15, Nr. 47 (1987).
15. T. L. Crawford, Numerical modelling of complex two- and three-dimensional flow and diffusion problems in the natural air environment. Ph.D. thesis, University of Waterloo, Canada (1977).
16. L. Pernecker, Une tentative de calcul tridimensionnel des champs de vitesse, de pression et de température autour d'un aérorefrigérant. EDF Report HE 041/79.03 (1979).
17. A. O. Demuren and W. Rodi, Three-dimensional numerical calculations of flow and plume spreading past cooling towers. *J. Heat Transfer* **100**, 113–119 (1987).
18. N. Hölscher, private communication (1988).
19. N. Hölscher and H. J. Niemann, Some aspects about the flow around a surface-mounted circular cylinder in turbulent shear flows. Proceedings of the 6th Symposium on Turbulent Shear Flows, Toulouse, 7–9 September (1987).
20. J. F. Thompson, Z. U. A. Wasi and G. W. Martin, *Numerical Grid Generation.* North-Holland, Amsterdam (1985).
21. P. S. Galpin, D. G. Raithby and J. P. Van Doormal, Discussion of upstream-weighted advection approximation for curved grids. *Numerical Heat Transfer* **9**, 241–246 (1986).
22. S. Majumdar and W. Rodi, Numerical calculation of turbulent flow past circular cylinders. Proceedings of the 3rd Symposium on Numerical and Physical Aspects of Aerodynamic Flows, Long Beach, California, 21–24 January (1985).
23. B. E. Launder and D. B. Spalding, The numerical computation of turbulent flows. *Comput. Methods Appl. Mech. Engng* **3**, 269–289 (1974).
24. W. Rodi, *Turbulence Models and Their Application in Hydraulics.* IAHR, Delft (1980).
25. W. Rodi, Examples of turbulence-model applications, in *Turbulence Models and their Applications,* Vol. 2. Editions Eyrolles, Paris (1984).
26. S. V. Patankar, Numerical Heat Transfer and Fluid Flows, Hemisphere Publishing, McGraw-Hill, New York (1980).
27. P. F. Galpin and G. D. Raithby, Solution of transport problems using general orthogonal control volumes. Progress Report to AECL, No. 308-13, December (1983).
28. J. P. Vandoormal and G. D. Raithby, Enhancements of the SIMPLE method for predicting incompressible fluid flows. *Numerical Heat Transfer* **7**, 147–163 (1984).
29. J. Counihan, An improved method of simulating an atmospheric boundary layer in a wind tunnel. *Atmosph. Envir.* **2**, 197–314 (1969).
30. R. Franke and B. Schönung, Die numerische Simulation der laminaren Wirbelablösung an Zylindern mit quadratischen oder kreisförmigen Querschnitten. Rept. SFB 210/T/39, University of Karlsruhe (1988).